



## Hydraulics of air–water flow in a supercritical bottom rack intake

S.N. Chan<sup>a,b</sup>, Colin K.C. Wong<sup>c</sup>, Joseph H.W. Lee<sup>a,\*</sup>

<sup>a</sup> Department of Civil and Environmental Engineering, The Hong Kong University of Science and Technology, Clear Water Bay, Hong Kong, China

<sup>b</sup> Institute for Advanced Study, The Hong Kong University of Science and Technology, Clear Water Bay, Hong Kong, China

<sup>c</sup> Civil Engineering and Development Department, Hong Kong Special Administrative Region Government, Hong Kong, China



### ARTICLE INFO

#### Keywords:

Supercritical flow  
Bottom rack  
Volume-of-fluid  
Computational Fluid Dynamics  
Air entrainment  
Storm water management  
Hydraulic structure

### ABSTRACT

A compact bottom rack structure is used for diverting storm water flow on steep catchments in the hinterland of a densely built city into a drainage tunnel through a vortex dropshaft. This study investigates the complex three-dimensional, turbulent and aerated flow of the bottom rack intake structure by comprehensive experiments and three-dimensional Computational Fluid Dynamics (CFD) modeling. Extensive physical model tests were conducted on a 1:9.5 Froude scale model over a wide range of discharges and different rack bar shapes. The water depth, velocity and air concentration were measured. As the rack interception induces an energy loss, the depth of the supercritical flow increases as it passes across the racks. The rack interception also gives rise to a sheet jet beneath it. In the rack chamber, the flow consists of a wall jet that impinges on a spiral circulation of aerated flow, inducing significant turbulence and air entrainment. The average air concentration ranges from 20% to 50% and decreases with increasing discharge. The air concentration in the chamber appears to be little affected by the presence of the bottom racks or the cross-sectional shape of the rack bars. The complex flow features and air concentration distribution in the rack chamber are satisfactorily predicted by the 3D numerical model.

### 1. Introduction

Hong Kong is frequented by tropical cyclones and experiences an average annual rainfall of 2400 mm. In recent years global climate change has also resulted in extreme rainfall intensity – for example, maximum hourly rainfall of 142 mm has been recorded on Hong Kong Island. To alleviate flooding and enhance flood protection standards, a storm water runoff interception and transfer scheme has been designed and constructed in the steep hinterland of its urban areas. The “up-stream diversion” scheme (the Hong Kong Island West Drainage Tunnel Scheme – HKWDT) involves the interception of stream flood flows above the urban and business districts for transfer to the sea in a drainage tunnel (DSD, 2003). The design consists of a 10.5 km long drainage tunnel (6.5 m diameter) fed by 34 vortex intake shafts (average height of around 80 m) positioned across the catchment basin. The intakes are located on steep hillslope water courses (average slope of 40%) with supercritical flow characterized by velocities in the order of 10 m/s (Froude numbers of  $F = U/\sqrt{gH} = 3\text{--}8$ , where  $U$  is the cross-section averaged velocity,  $H$  is the flow depth and  $g = 9.81 \text{ m/s}^2$  is the gravitational acceleration). During significant storm events, stream flows often carry sediments, boulders and/or debris. The HKWDT scheme is designed for a 1 in 200-year return period rainstorm event, with an intake design discharge of up to  $18 \text{ m}^3/\text{s}$ .

Each intake intercepts and transfers stormwater runoff to the main tunnel through a vertical drop shaft. The design of such an intake structure adjacent to densely populated residential areas (including some premium properties) is an engineering challenge. A bottom rack intake is proposed to intercept the supercritical flow. The intercepted flow is then passed into the dropshaft via a bottom rack chamber which changes the flow direction by 90 degrees, and a vortex inlet. The change in flow direction is required because of site constraints; the vortex inlet facilitates energy dissipation and the development of a central air core within the dropshaft. Both upstream of the bottom rack intake or within the structure, the flow cannot be fully stilled because of site constraints; the intercepted flow remains supercritical throughout the structure.

A bottom rack is a hydraulic structure provided at the bottom of a channel for flow diversion. It consists essentially of an opening in the channel bottom covered with an arrangement of metal racks to prevent the transport of debris or sediment through the opening. Bottom racks are used for hydropower, water supply and irrigation, mainly in areas with steep terrain and gravel river beds (e.g. Subramanya, 2009). However, previous studies are mainly concerned with sub-critical approach flows (e.g. Mostkow, 1959; Brunella et al., 2003; Hager and Minor, 2003; Righetti and Lanzoni, 2008; Kumar et al., 2010).

The present bottom rack chamber design was derived from a

\* Corresponding author.

E-mail address: [jhwlee@ust.hk](mailto:jhwlee@ust.hk) (J.H.W. Lee).

<https://doi.org/10.1016/j.jher.2018.08.001>

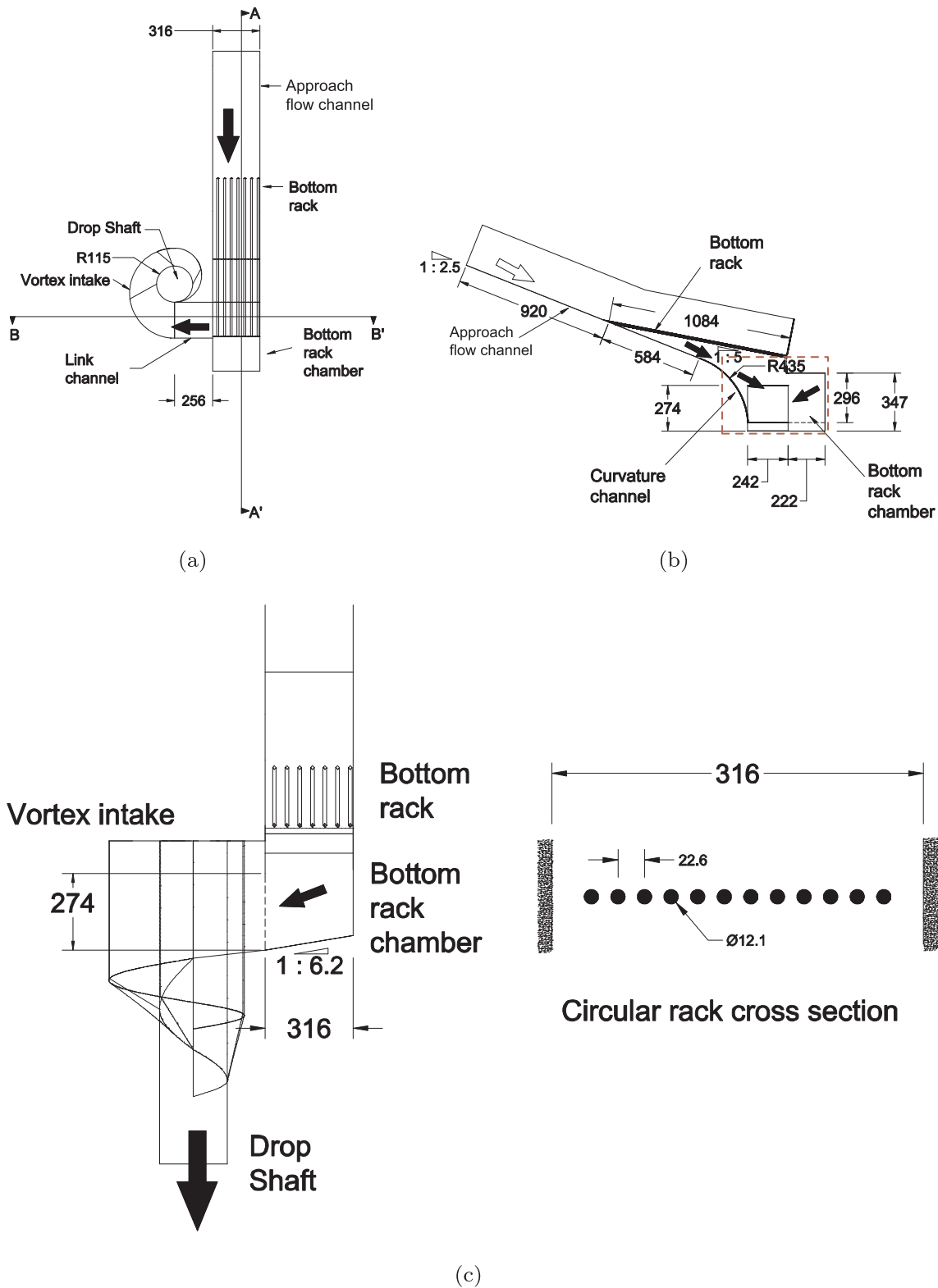


Fig. 1. Experimental set-up of 1:9.5 bottom rack model (unit: mm), (a) top view, (b) section A–A, (c) section B–B and rack arrangement.

comprehensive physical model investigation (Lee et al., 2005a), and is significantly different from standard designs in several ways. First, the approach flow is supercritical and remains so after rack interception; the channel bottom also forms part of the bottom rack chamber. Second, in a standard design the flow above the rack is essentially a spatially varied flow with decreasing discharge; the flow downstream of rack interception plunges into empty space below as a free overfall. In

the present design, the flow above the rack plunges onto the underlying supercritical channel flow, and the rack bars also create complex flows such as sheet jets beneath the rack bars. The interaction of the channel flow and the sheet jet with the chamber flow have not been studied. Third, the rack chamber is relatively compact and designed for flow diversion with stable energy dissipation. Aeration is expected to be an important flow feature; such complex turbulent aerated flows in bottom

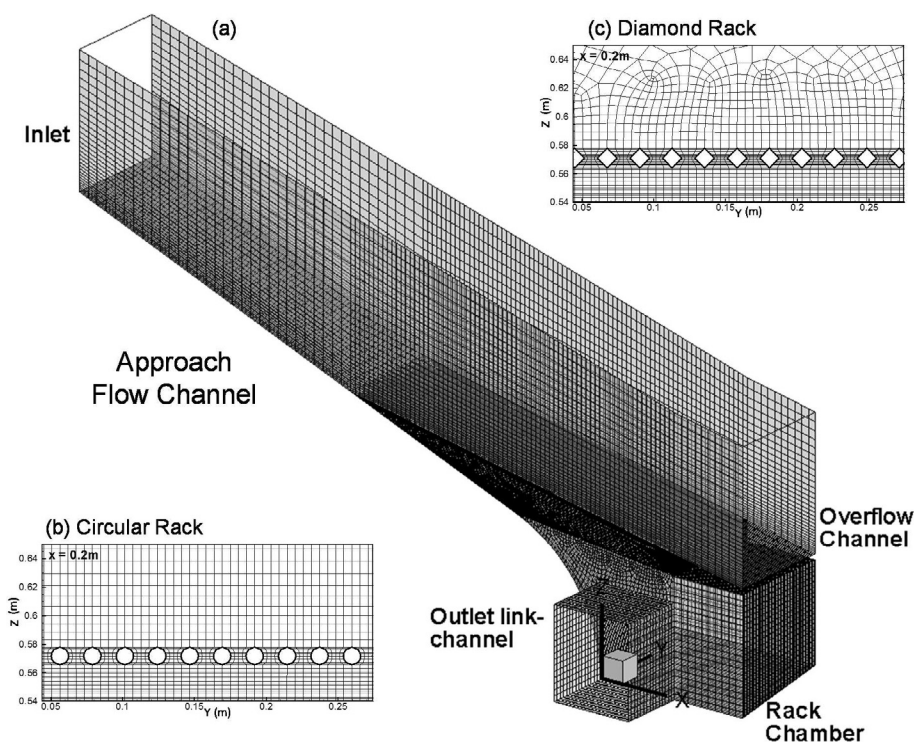


Fig. 2. (a) Computational mesh of laboratory model of supercritical bottom rack intake, (b) mesh details at the cross section of circular rack bars, (c) mesh details of diamond rack bars.

rack chamber have not been systematically studied.

In recent years, attempts have been made to tackle the air–water flow in bottom racks using Computational Fluid Dynamics (CFD) models with the Volume-of-Fluid (VOF) method. The air–water interface is located and tracked when it moves through the computational domain. Two-dimensional (2D) CFD prediction on stepped spillways has been performed to study the flow, turbulence and the on-set criteria for air entrainment (Bombardelli et al., 2011; Meireles et al., 2014), using the commercial code FLOW-3D. The numerical prediction has also been compared with an open source CFD code OpenFOAM (Bayon et al., 2017). Despite the satisfactory comparison of model predicted free surface and velocity field with laboratory measurement in the non-aerated region of stepped spillway, the flow features in the aerated regions, in particular the air concentration, have not been successfully predicted. Valero and Bung (2015) attempted a three-dimensional (3D) VOF CFD prediction on the aerated region of a stepped spillway using FLOW-3D, but the predicted air concentration distribution failed to compare satisfactorily with the measured data. This may be attributed to the formulation of the FLOW-3D code which only computes the water flow and does not solve the air flow (assuming negligible inertia, Bombardelli et al., 2001), thus a semi-empirical air entrainment model (Hirt, 2003) is required as a boundary condition for the free water surface. For the study of supercritical bottom rack flow, a 3D CFD simulation using VOF was previously attempted (Wong, 2009); however the details of the air–water interactions induced by the bottom racks could not be resolved by the coarse grid resolution. More recently Castillo et al. (2013) used the VOF method to simulate the flow across a bottom rack; the numerical computations for subcritical approach flows were validated with experimental data. Nevertheless, there is scant numerical or experimental work on bottom racks with supercritical approach flows; the complex air–water interactions have also not been studied.

As far as we are aware, this study is the first systematic investigation of air–water flow in a bottom rack used for urban stormwater management. This paper presents a detailed experimental and CFD study on the hydraulics of the supercritical air–water flow in a bottom rack. First,

the physical experiment set-up and the bottom rack chamber design are described along with the experimental measurements. Second, the CFD model set up for the bottom rack chamber including the rack bars is presented. Third, the experimental and numerical results are compared and discussed.

## 2. Experiments

### 2.1. Design of bottom rack chamber

The objective is to arrive at a design that ensures stable flow diversion up to the maximum 200-year flood discharge. Because of very tight space constraints the design of a compact diversion structure is most challenging. An undistorted Froude scale model was used to study the hydraulics of the bottom rack and chamber flow (Lee et al., 2005a). A series of experiments was performed to study many candidate designs for  $Q = 1\text{--}18\text{ m}^3/\text{s}$  (Lee et al., 2005b). It was found that the complex bottom rack flow behaviour depends on (i) the length and slope of the approach channel; (ii) the slope, length and arrangement of the bottom rack bars; and (iii) the length and slope of the channel bed, and the volume and geometry of the rack chamber. Designs which resulted in unstable strong rollers and/or undesirable flow overshoot onto the downstream channel were not acceptable. Fig. 1a- and b- show, respectively, the top and longitudinal section views of the design of a 1:9.5 bottom rack model (made of perspex) adopted after extensive model testing. The bottom rack structure comprises the approach flow channel, the longitudinal rack bars (aligned parallel to the flow), the bottom rack chamber, and the link channel leading into the vortex intake. The approach flow channel has a bottom slope of 1:2.5, and the flow is intercepted by a bottom rack in 1:5 slope. The channel bottom beneath the rack follows a curved boundary (resembling a free jet trajectory) at the entrance to the bottom rack chamber (Fig. 1b). Fig. 1c shows the cross-sectional view of the rack bars, and the connection of the bottom rack with the vortex intake. Downstream of the bottom rack chamber, the flow is diverted by 90° to the vortex intake structure via the link-channel (Fig. 1a and c). Comprehensive experiments at 1:24.5

and 1:9.5 scales were performed separately for the bottom rack chamber, vortex intake, and then the integrated bottom rack chamber and vortex intake. Details of the experimental investigations on different candidate designs are provided in Lee et al. (2005a,b, 2006). While circular bars were adopted for the baseline design, different cross-sectional shapes were also tested, including circular, diamond, I-beam and trapezoidal bars. Circular racks were made of 12.1 mm diameter bars with 22.6 mm center-to-center separation, while diamond racks were made of  $8.4 \times 8.4$  mm square bars with 23 mm center-to-center separation. Fig. 2 shows the 3D computational mesh for the physical model of the bottom rack chamber up to the outlet of the bottom rack chamber on the supercritical link channel.

## 2.2. Physical model tests

The experiments were conducted under steady flow conditions; a recirculating flow system could be set up with the inflow supplied from a constant head tank (reservoir) at the upstream entrance to the steep approach flow channel, and the outflow discharged into a laboratory sump tank. The inflow was monitored by two calibrated ultrasonic flowmeters (Controlotron 1010P, Advanced Test Equipment Corp, San Diego, CA). A total of 50 model tests were performed for discharges from 14.6 to 70.5 L/s; detailed measurements were conducted for three representative nominal flow rates:  $Q \approx 22, 43$  and 65 L/s. The key flow observations were recorded by a digital camera and/or a video-camera. The experimental measurements were made in three zones: (i) above the rack, (ii) downstream of rack interception but before the flow detaches completely from the rack bars; and (iii) inside the rack chamber (cf. Fig. 3). The flow depth profile above the rack was measured by a point gauge mounted along the channel axis and perpendicular to the channel bed, at a streamwise interval of 25 mm. The wetted length along the bottom rack was also measured from the tip of the rack by a steel rule.

Downstream of rack interception, the flow depth, velocity and air concentration were measured. The flow depth beneath the rack was observed on the transparent channel side wall. A calibrated high-speed propeller current meter (NIXON type 404) was used to measure the flow velocity above the rack and between the racks along the channel axis at 5 mm vertical intervals. The air concentration was measured by two in-house developed single tip conductivity probes (one between the racks, one immediately beneath the rack bar). The measurement by the conductivity probe between the rack was also cross-checked with a double tip fiber-optical probe (RBI Instrumentation). The air concentration within the bottom rack chamber was measured by a conductivity probe on three vertical planes: near the wall, at the channel axis and near the outlet of the chamber – at 5 mm vertical intervals and with a sampling period of 20 s (sampling rate at 20 kHz). Measurements were made on four transects on each plane (i.e. total of 12 vertical air concentration profiles). A detailed calibration test using an ‘air–water’ jet (with controlled source air concentrations) indicated that both optical and conductivity probes provide good repeatability and accuracy of around 7% and 10–15%, respectively. Details of the physical model experiments and measurement techniques are provided in Wong (2009).

## 3. Computational Fluid Dynamics model

### 3.1. Governing equations

The VOF method models two immiscible fluids (water and air) by solving a single set of momentum equations and tracking the volume fraction of each fluid throughout the computational domain (Hirt and Nichols, 1981). The tracking of the interface between the phases is accomplished by the solution of a continuity equation for the volume fraction of one of the phases. For the water phase, this equation has the following form:

$$\frac{\partial}{\partial t}(\alpha_w \rho_w) + \nabla \cdot (\alpha_w \rho_w \mathbf{U}) = 0 \quad (1)$$

where  $\alpha_w$  is the volume fraction for the water phase. The volume fraction for the air phase  $\alpha_a$  is computed based on the constraint:

$$\alpha_a + \alpha_w = 1$$

In a two-phase system, the phase-averaged density and molecular viscosity in each cell are given by:

$$\rho = \alpha_w \rho_w + (1 - \alpha_w) \rho_a \quad (2)$$

$$\mu = \alpha_w \mu_w + (1 - \alpha_w) \mu_a \quad (3)$$

where the densities of air and water are treated as constant of  $\rho_a = 1.225 \text{ kg/m}^3$  and  $\rho_w = 998.2 \text{ kg/m}^3$ , respectively, and the dynamic viscosity of air and water are  $\mu_a = 1.8 \times 10^{-5} \text{ kg/m/s}$  and  $\mu_w = 1.0 \times 10^{-3} \text{ kg/m/s}$ , respectively.

A single momentum equation is solved throughout the domain, and the resulting velocity field  $\mathbf{U} = (u, v, w)$  is shared among the phases. The momentum equation below depends on the volume fractions of all phases through the properties  $\rho$  and  $\mu_i$ :

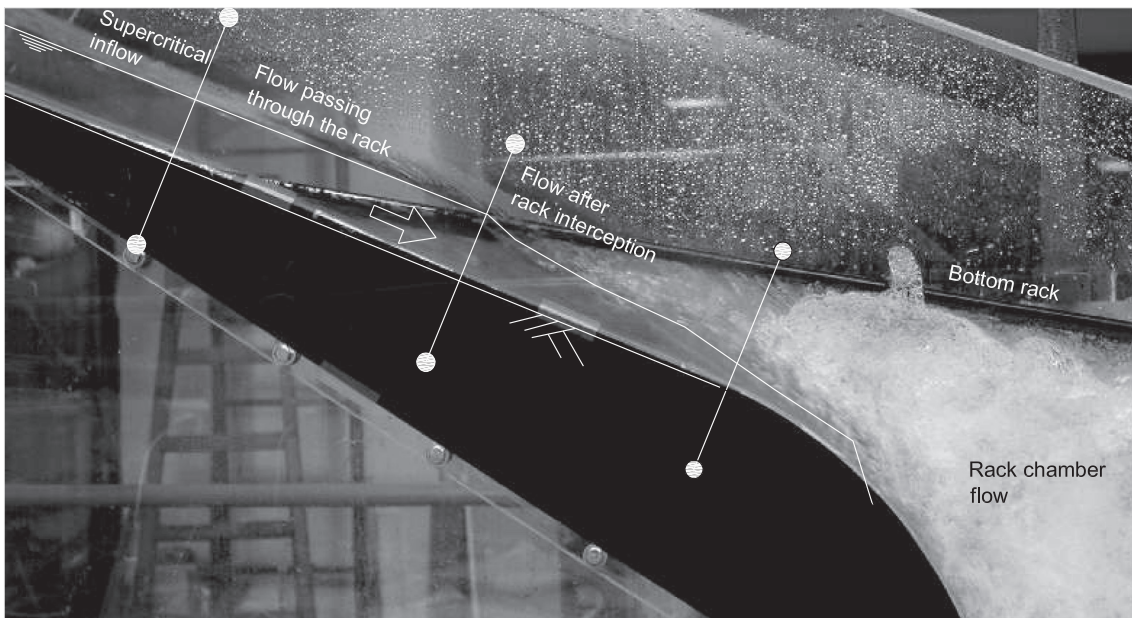
$$\frac{\partial}{\partial t}(\rho \mathbf{U}) + \nabla \cdot (\rho \mathbf{U} \mathbf{U}) = -\nabla P + \nabla \cdot [\mu_i (\nabla \mathbf{U} + \nabla \mathbf{U}^T)] + \rho \mathbf{g} \quad (4)$$

where  $\mathbf{g} = (0, 0, 9.81) \text{ m/s}^2$  is the gravitational acceleration. The phase-averaged turbulent dynamic viscosity  $\mu_i$  is determined using the Re-Normalisation Group (RNG)  $k-\epsilon$  turbulence model for the air–water mixture (Yakhot et al., 1992), which has been shown to produce better results for swirling and recirculating flows.

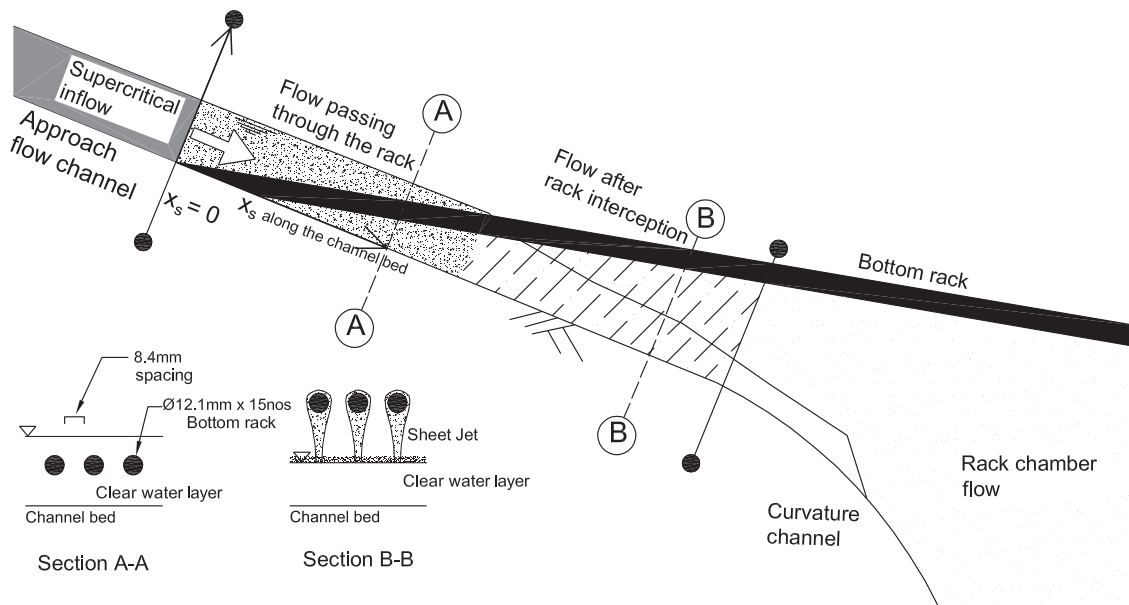
The governing Eqs. (1) and (4) are solved numerically using the finite volume method in the commercial CFD code of ANSYS FLUENT 15 (ANSYS, 2013). The PISO (Pressure-Implicit with Splitting of Operators) algorithm is employed for velocity–pressure correction with an under-relaxation factor of 0.5 for pressure and momentum, 0.2 for volume fraction of water, 0.8 for  $k$  and  $\epsilon$ , and 1.0 for density and turbulent viscosity. A second order upwind advection scheme is used for momentum and density, while a first order upwind advection scheme is used for  $k$  and  $\epsilon$ . The volume fraction equation (Eq. 1) is spatially discretized using the Modified High Resolution Interface Capturing (HRIC) Scheme in FLUENT, which provides improved accuracy for VOF calculations for the implicit solution of the volume fraction (with less stringent requirement for stability than using an explicit solver). A first order implicit time stepping scheme is used for the marching of solution with time. Convergence is declared if the normalized residual is less than  $10^{-4}$  for all variables. Typically about 10 iterations are required for convergence in each time step. The VOF model in the FLUENT code has been successfully used in the numerical modeling of air–water interaction leading to explosive geysers in pressurized drainage tunnels (Chan et al., 2018).

### 3.2. Model grid, boundary conditions and other computational details

The CFD model is set up in exact accordance with the physical model of the bottom rack – from the reservoir entrance at the upstream end of the approach flow channel to the outlet of the bottom rack chamber (Fig. 1). Note that although the bottom rack is designed for 100 percent interception, any un-intercepted flow above the rack bars would flow downstream via an overflow channel. The modeling focuses on the experiment with circular and diamond shaped rack bars, as these two are considered to be better designs (in terms of flow interception) as compared with bars with I-beam and trapezoidal shapes (Wong, 2009). An unstructured boundary-fitted model grid is used for numerical simulation (Fig. 2a). The number of grid cells ranges from 67,840 for cases without the bottom rack to 347,520 for cases with circular rack bars. Mesh refinement is made near the bed and the region of bottom rack (Fig. 2 insets). The minimum grid size is around  $\sim 1$  mm. As the outflow from the bottom rack is supercritical the vortex intake



(a)



(b)

Fig. 3. Observed flow features of the bottom rack flow: (a) side view ( $Q = 64.1 \text{ L/s}$ , circular rack), (b) key flow regimes and characteristics..

and its linkage channel are not included in the CFD model. The computational model has four open boundaries – the inflow, the outflow to the link channel for the vortex dropshaft, the overflow outlet and the top atmospheric boundary. The upstream inlet of the approach flow channel is prescribed with the total water flow rate and the critical depth. The upper boundary of the CFD model is prescribed with zero gauge pressure. The outlets of overflow channel and the link channel are prescribed with zero gauge pressure as the water depth is not known beforehand. A roughness height of 0.01 mm is prescribed for all wall

and solid boundaries. The model is run from an initially dry condition. The supercritical flow in the approach flow channel and the bottom rack chamber develops from the inlet with a time step of 0.0005 to 0.001 s. The initial start-up period is about 10 s and afterwards the model prediction is considered quasi-steady. About 20 s of quasi-steady state solution, at a time interval of 0.1 s, is used for evaluating the time-averaged properties for flow depth, velocity and air concentration. The run time for 20s of flow ranges from  $\approx 15 \text{ h}$  for cases without bottom rack to  $\approx 120 \text{ h}$

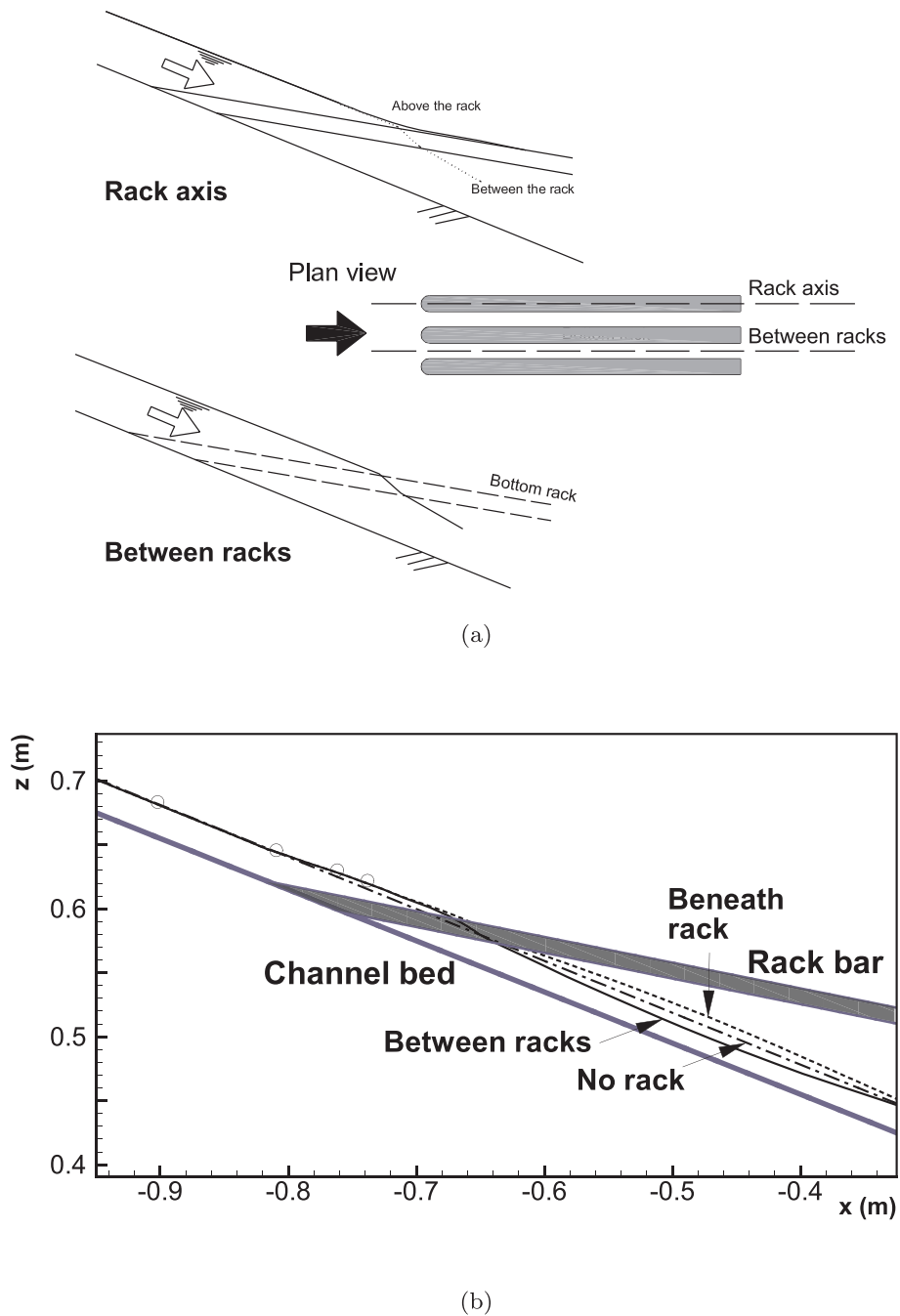


Fig. 4. (a) Observed and (b) CFD predicted flow ‘between the rack’ and ‘above the rack’ ( $Q = 45.4 \text{ L/s}$ , circular rack). Predicted free surface ( $Q = 43.1 \text{ L/s}$ ) is represented by the 50% air concentration line. Symbols are measured free surface before the rack.  $x$  = horizontal distance from the corner of chamber at toe of curved channel (see Figs. 1 and 9).

(5 days) for cases with the bottom rack, on a Dell workstation with an Intel i7-6700 3.4 GHz CPU with quad-core parallel computation. Numerical simulations are performed for four representative flow rates:  $Q = 21.6, 41.3, 43.1,$  and  $70.5 \text{ L/s}$ , and three rack bar types: without rack, circular and diamond shaped bars.

#### 4. Comparison of numerical model and experimental results

##### 4.1. Flow profile above the bottom rack

Fig. 3 shows the observed bottom rack flow. The flow profile upstream of the bottom rack follows a typical S2 curve (Henderson, 1966). Gradually varied flow computations (which are in excellent agreement

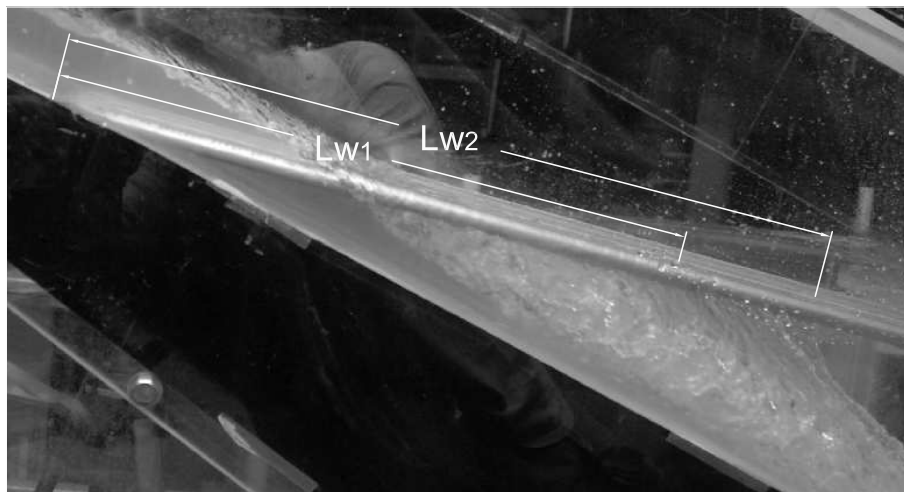
with the data) show that the depth at the point of incipient interception ( $x_s = 0$ , at the location of the leading edge of the bottom rack) is greater than the normal depth – i.e. normal flow is not reached (Wong, 2009). Downstream of  $x_s = 0$ , the flow enters the rack chamber in the space between the rack bars (Fig. 3). The flow above the rack is bounded by  $L_w$ , the distance (along the rack) between  $x_s = 0$  and the point where the free surface intersects the rack. This distance is also used to define the minimum required length of the rack for complete flow interception.

Fig. 3a shows that there is no choking or hydraulic jump above the rack; the upstream flow penetrates between the bars to form an underflow that runs along the channel bed. Due to the existence of a shockwave pattern on the surface of the supercritical flow, the

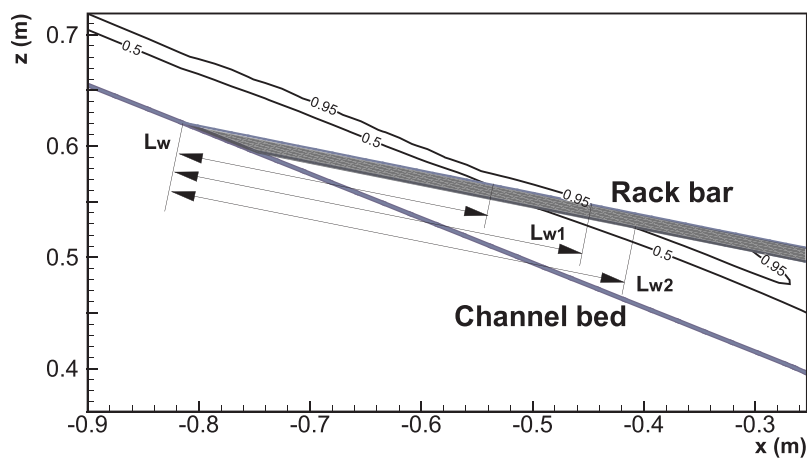
**Table 1**

Measured and predicted wetted lengths ( $L_w$ ,  $L_{w1}$ ,  $L_{w2}$ ) for bottom rack of different shapes. Note that  $L_{w1}$  for I-beam and trapezoidal bars is not applicable as water flows on the rack surface until it reaches the end of the bar. CFD prediction for the high flow case is for  $Q = 70.5$  L/s.

Discharge $Q$ (L/s)	Wetted lengths	Measured (mm)				Predicted (mm)	
		Circular	Diamond	I-beam	Trapezoidal	Circular	Diamond
21.6	$L_w$	112	125	180	160	161	151
	$L_{w1}$	240	350	–	–	226	250
	$L_{w2}$	420	545	660	520	300	339
43.1	$L_w$	212	225	280	230	226	276
	$L_{w1}$	450	365	–	–	344	391
	$L_{w2}$	510	560	780	660	388	498
64.7	$L_w$	275	325	330	310	380	393
	$L_{w1}$	580	510	–	–	435	507
	$L_{w2}$	670	690	810	740	483	520



(a)



(b)

**Fig. 5.** (a) Observed flow and (b) predicted air concentrations in aeration flow downstream of flow interception by rack (longitudinal centerline section), and definition of wetted rack lengths  $L_{w1}$  and  $L_{w2}$  (circular rack,  $Q = 43.5$  L/s).

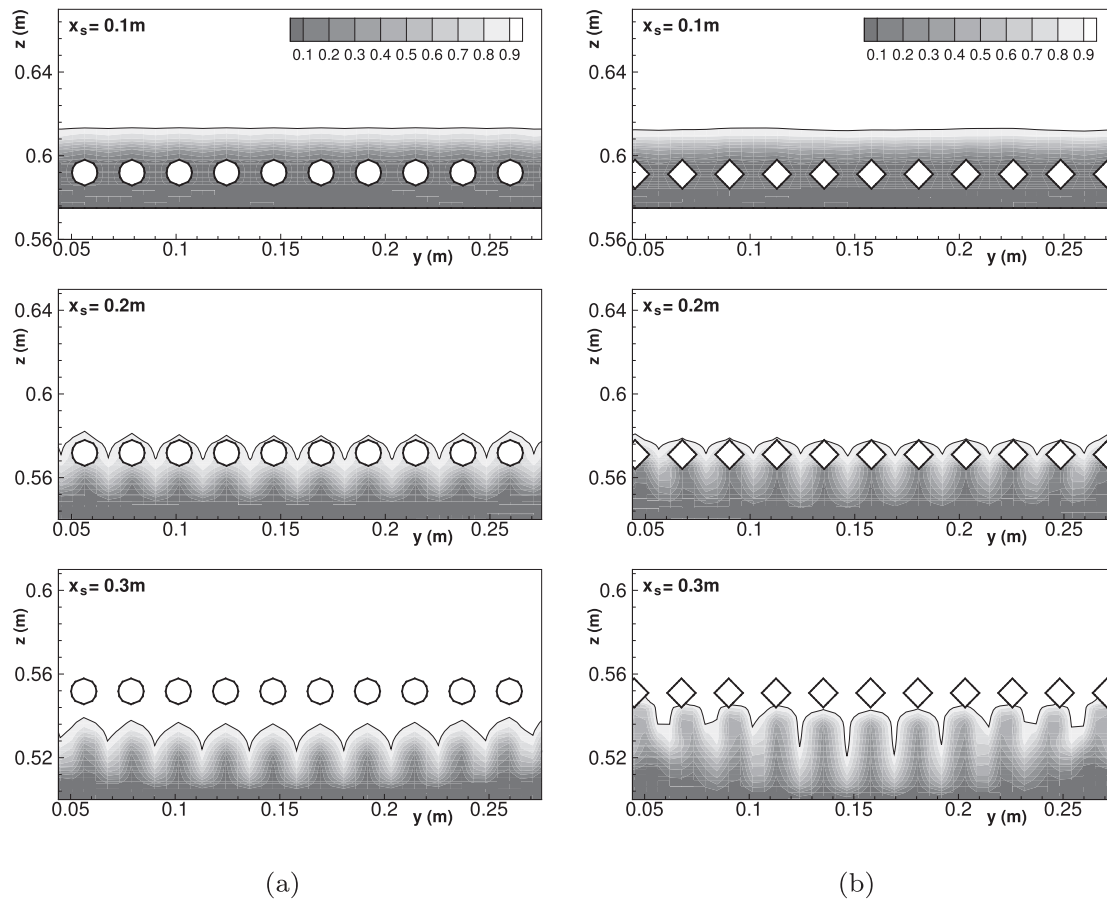


Fig. 6. Predicted air concentration at rack cross sections downstream of rack interception,  $Q = 23.6 \text{ L/s}$ : (a) circular rack, (b) diamond rack..

maximum variation of flow depth in the transverse direction is around 2–5% of the mean depth. Fig. 4 compares the flow depth for two cases: (a) in the presence of, and (b) without the rack. For (a), the flow depth rises higher than that without rack; near the tip  $x_s \approx L_w$  the free surface appears to be asymptotic to the slope of the bar. At  $x_s \approx 0.5L_w$ , the flow depth has increased around 8–22%. For  $x_s \leq 0.75L_w$ , the free surface level is well-predicted by the Gradually-varied flow theory using the Standard Step Method (e.g. Henderson, 1966; Subramanya, 2009) and assuming an eddy loss coefficient of 0.4 (energy loss due to racks proportional to the local velocity head) (Wong, 2009). Near the end of  $L_w$ , the flow depth between the rack drops rapidly because of the absence of the rack effect. In general, for  $x_s \leq L_w$  the flow depths ‘between the rack bars’ and ‘directly above the rack bar’ are similar. CFD predictions of the free surface level (defined as 50% air concentration) shows a good comparison with the data. The predicted and measured lengths of interception on the bottom rack,  $L_w$ , are compared for different rack shapes (Table 1). Note that circular and diamond-shaped rack bars result in the smallest  $L_w$  for all three flow rates (i.e. minimum required length of bottom rack chamber).

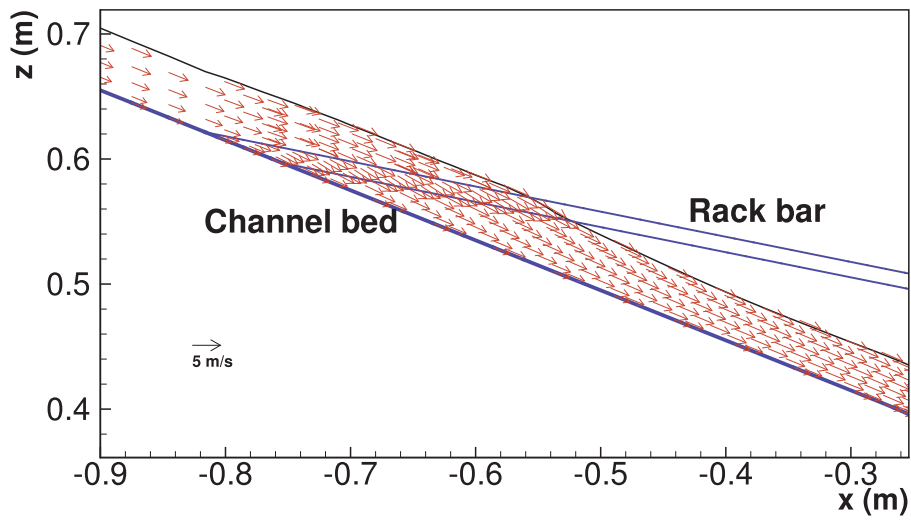
In previous bottom rack studies (e.g. Brunella et al., 2003), the flow falls freely between the rack bars into an open space below before being diverted to a collection channel or chamber. The use of a head-discharge relation to quantify the local side discharge is hence valid and enables the prediction of the spatially varied flow above the rack. However, for the present design, the channel flow runs through the rack opening and continues as a wall jet along the curved bottom boundary into the chamber. In addition to bottom friction, significant energy loss is induced by the flow contraction and expansion due to the rack, and the impingement of the wall jet onto the recirculating bottom chamber flow.

#### 4.2. Channel flow profile downstream of rack interception

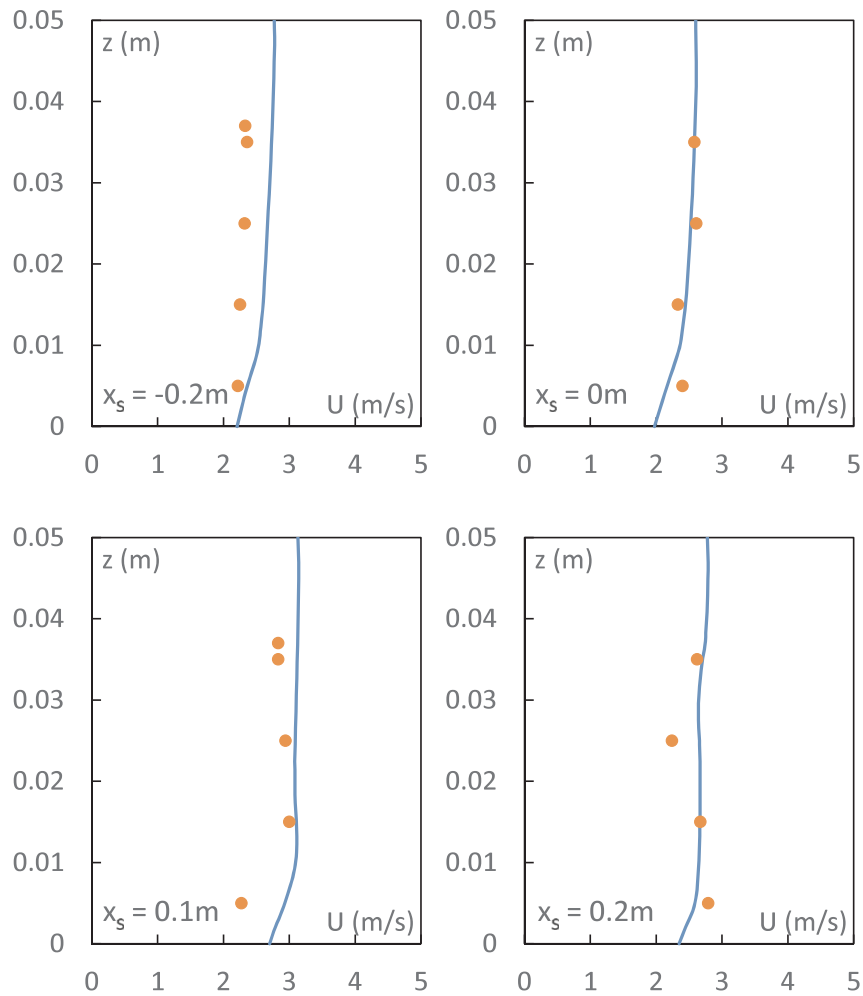
The rack splits the approach flow into two streams: (i) the main channel flow, and (ii) the attached rack flow. The main channel flow is supercritical along the channel with an S2 profile. For  $x_s > L_w$ , due to the forward momentum, the fluid still clings onto the rack bar, and a small part of the flow is attached to and runs along the surface of the bottom rack before leaving the rack at high speed and forming a thin sheet-jet beneath the rack (Fig. 5a). Disintegration of this sheet jet in air is observed as it plunges onto the main channel flow; the free surface of the channel flow beneath the rack is irregular.

In addition to  $L_w$ , two wetted lengths of bottom rack ( $L_{w1}$  and  $L_{w2}$ ) are measured to further quantify the longitudinal extent of the flow interception (Fig. 5a):  $L_{w1}$  is the distance at which the top of the rack bars is no longer wetted;  $L_{w2}$  is the distance where the flow attached to the rack bars (bottom) eventually stops. The experimental measurements of  $L_{w1}$  and  $L_{w2}$  for different rack shapes are given in Table 1. It can be seen that for all the three flow rates tested, the circular and diamond racks produce significantly smaller  $L_{w1}$  and  $L_{w2}$  compared with the other two rack shapes. This is due to the flat top surfaces of I-beam and trapezoidal bars, allowing for the flow to cling onto the top surface of the bar over the entire bottom rack length. The flat top-surface results in more overflow to the downstream channel, which is not desirable. Based on these results, the circular rack is selected to be the optimal bottom rack type as it possesses the shortest  $L_{w2}$  length without overflow discharge.

Fig. 5b defines  $L_w$ ,  $L_{w1}$  and  $L_{w2}$  from the CFD predicted air concentration.  $L_w$  is the length from the rack start to the location where the 50% air concentration contour intersects the top of rack bar, which represents the main interception length.  $L_{w1}$  is defined as the length

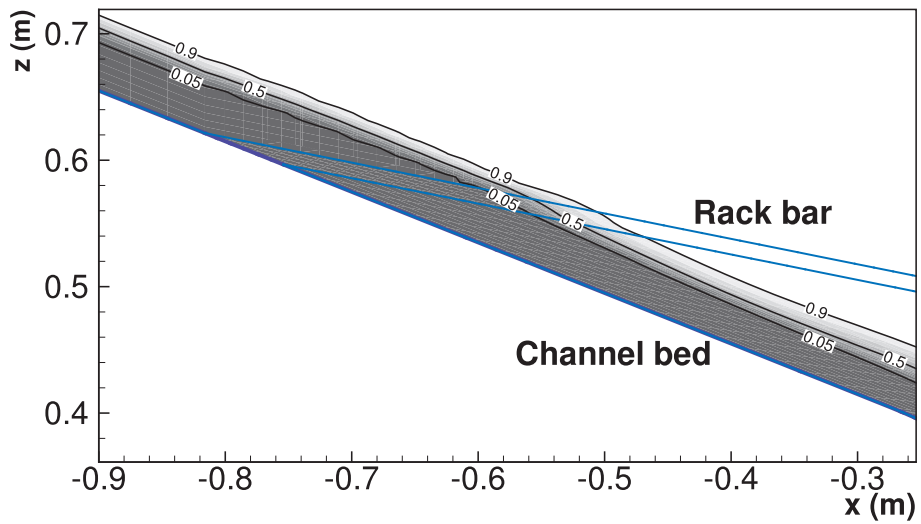


(a)

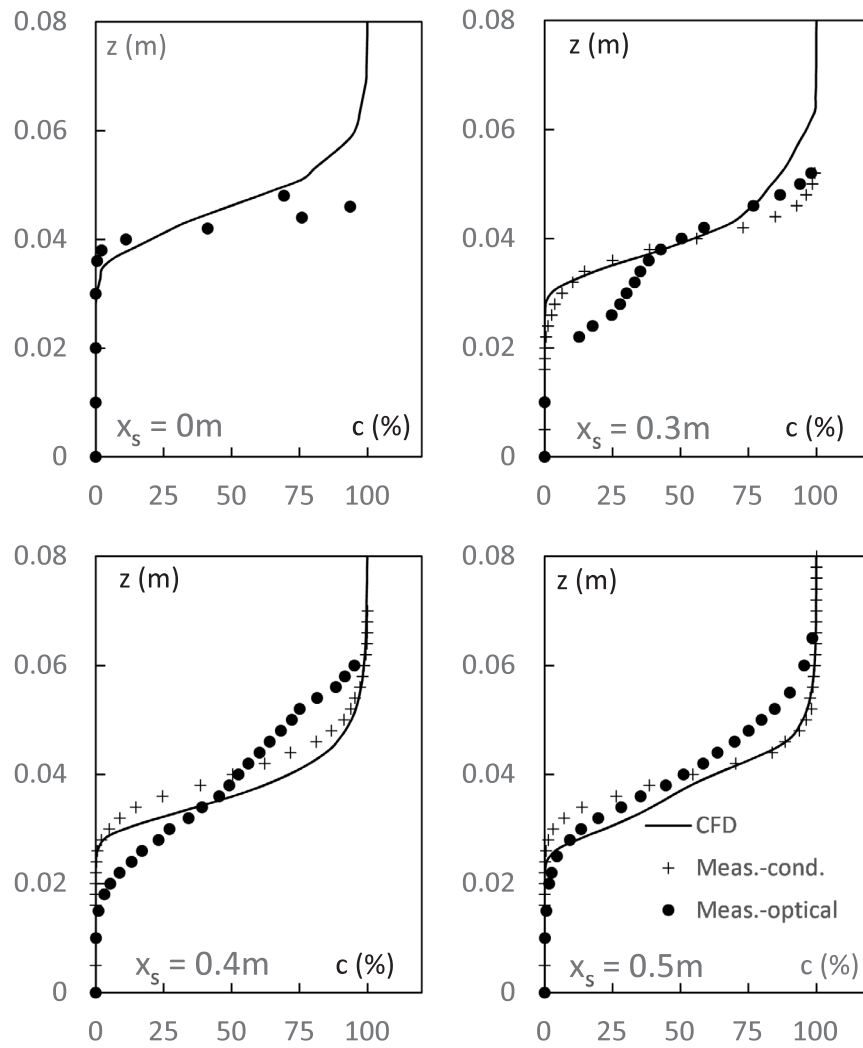


(b)

Fig. 7. (a) CFD predicted velocity field between racks ( $Q = 41.3L/s$ , circular rack). Predicted free surface is represented by the 50% air concentration line. (b) Comparison of predicted and measured velocity profile at different cross sections.

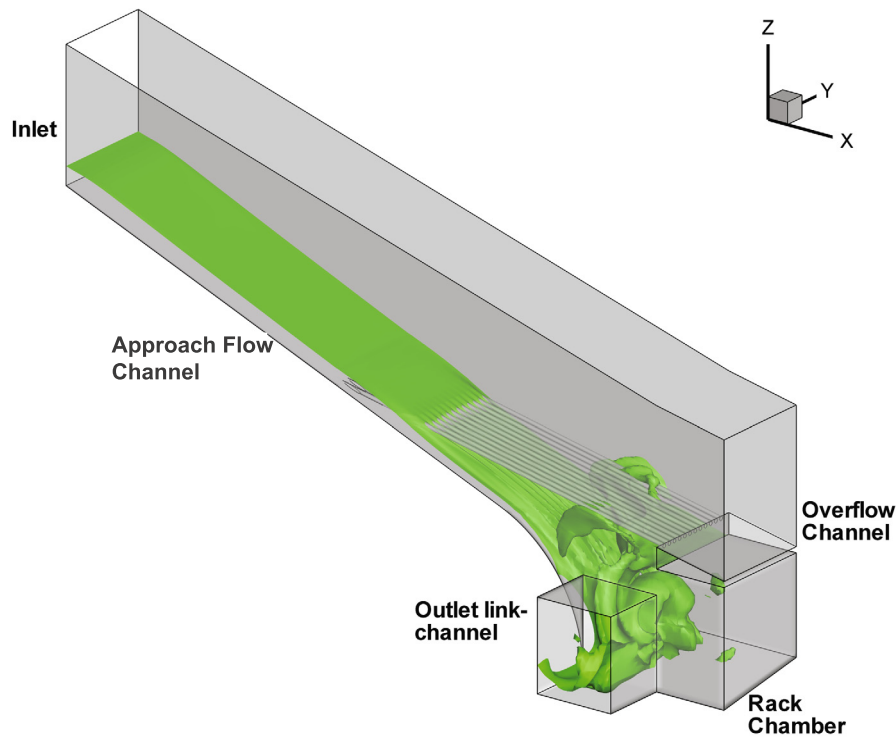


(a)



(b)

**Fig. 8.** (a) CFD predicted air concentration between racks ( $Q = 41.3L/s$ , circular rack), (b) comparison of predicted and measured air concentrations (by conductivity and optical probes) at different cross sections.



(a)



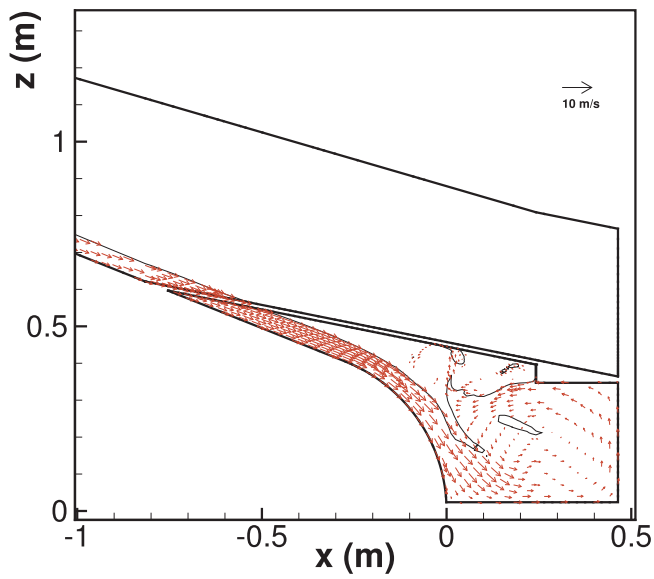
(b)

**Fig. 9.** CFD predicted and observed flow features at the rack chamber for medium flow ( $Q = 43.1 \text{ L/s}$ ): (a) 3D view of free surface (50% air concentration), (b) observed flow features.

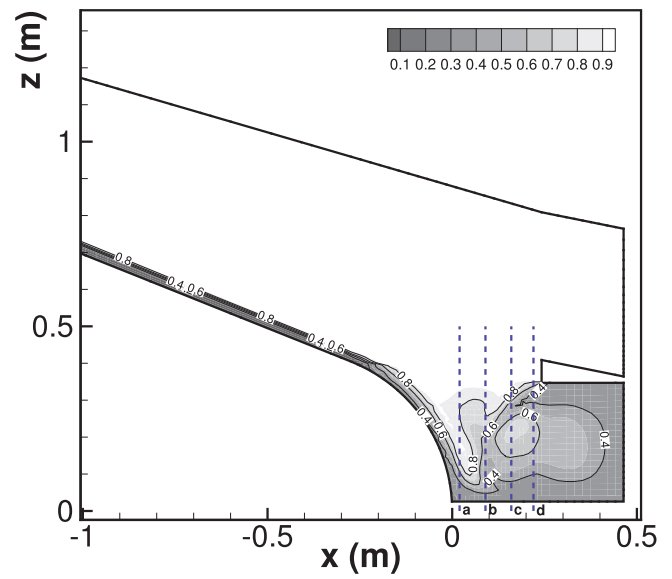
from the rack start to the location where the 95% air concentration intersects the top of rack bar, which represents the thin water layer wetting the rack surface.  $L_{w2}$  is defined as the length from the start of rack to the location where 95% air concentration contour intersects the bottom of rack bar, representing the end of the sheet jet. The predicted wetted lengths are shown in Table 1. In general the prediction of  $L_w$  is in good agreement with measurement, with an average error of 22% (diamond shape) to 26% (circular); however the model under-predicts  $L_{w1}$  and  $L_{w2}$ , reflecting the difficulty in simulating the dynamics of this thin layer flow with the present realistic grid resolution (1–2 grid cells over the depth).

Fig. 6 shows the predicted air concentration distribution in a cross section perpendicular to the rack for  $Q = 23.6 \text{ L/s}$ , for circular and diamond shaped rack bars, respectively. Note that upstream of full flow interception ( $x_s = 0.1 \text{ m}$ ), the predicted air concentrations are similar for both rack shapes considered. Rack interception occurs between

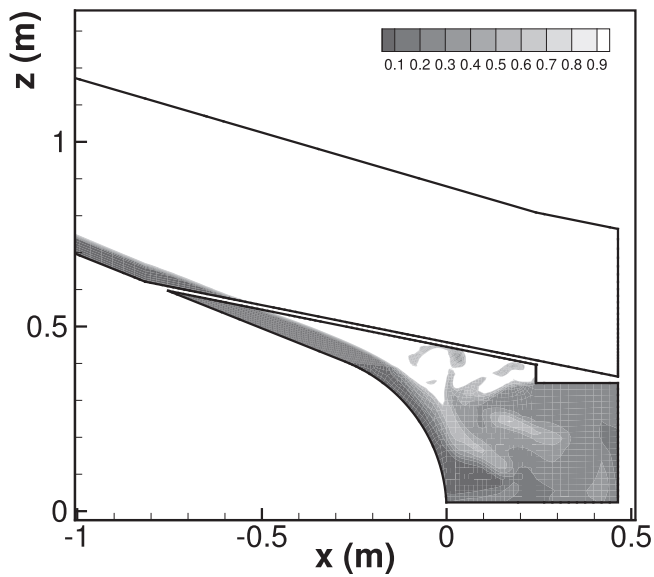
$x_s = 0.1\text{--}0.2 \text{ m}$ , which is consistent with the measured  $L_w$  ( $\approx 120 \text{ mm}$ ) for both rack shapes (Table 1). At  $x_s = 0.2 \text{ m}$ , the air concentration increases to about 0.9 just above the top rack surface. Although the details of the free surface around the rack bars cannot be resolved by the model grid (a prohibitively small grid size would be required to simulate the thin sheet flow), this location can be considered as length  $L_{w1}$  where the top of rack bars ceases to be wetted. The predicted  $L_{w1}$  location is consistent with the measurement (240–350 mm). Finally at  $x_s = 0.3 \text{ m}$ , for the circular rack, the contour lines of  $c = 90\%$  detached significantly from the rack bars, while for diamond rack, the  $c = 90\%$  are still mostly attached to the bottom surface of the rack. This is also consistent with the observed  $L_{w2}$  length with a longer attachment length of the diamond rack. The predicted air concentration has a ‘peak-and-trough’ structure where the air concentration is lower ‘beneath the rack bars’ than that ‘between the rack bars’. This phenomenon resembles the ‘sheet jet’ observed beneath the rack bars although the



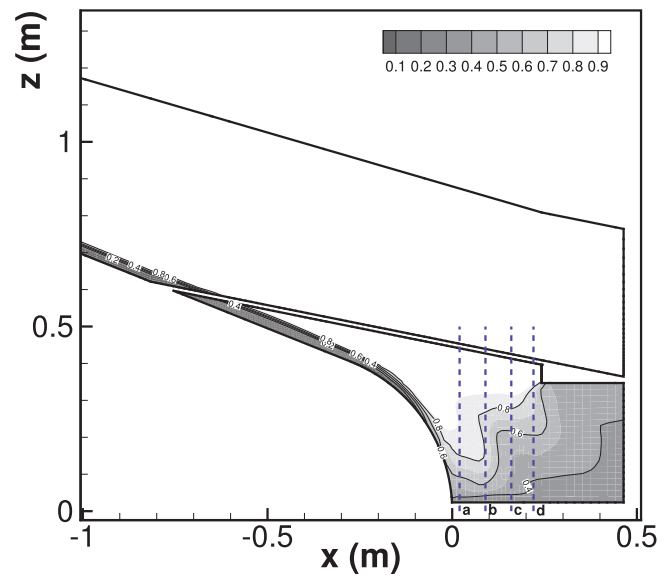
(a)



(a)



(b)



(b)

Fig. 10. CFD predicted (a) instantaneous velocity, (b) instantaneous air concentration at the rack chamber for medium flow ( $Q = 43.1$  L/s).  $x = 0$  refers to the toe of curved channel at the bottom of chamber.

Fig. 11. CFD predicted average air concentration distribution along centerline of bottom rack chamber for low flow ( $Q = 23.6$  L/s), (a) without rack, (b) circular-bar rack.  $x = 0$  refers to the toe of curved channel at the bottom of chamber.

details of such a thin layer of flow cannot be resolved in the CFD model.

#### 4.3. Channel flow field beneath rack

The entire bottom rack flow can be illustrated by the computed velocity field in the longitudinal centerline section between the rack bars (Fig. 7a) for a medium flow of  $Q = 41.3$  L/s; predicted streamwise  $x_s$ -velocity profiles at several cross-sections are also compared with experimental measurements (Fig. 7b). The supercritical open channel flow is intercepted by the rack; the flow contraction and expansion at the rack opening induces energy dissipation, resulting in a slight increase in depth. The maximum velocity occurs where the flow leaves the rack. Downstream of rack interception, the clear water flow runs along the main channel with a decreased depth as it accelerates without

obstruction, with a zone of air–water mixture above (due to the plunging sheet flow from the rack bars). Comparing with the flow for other rack shapes (diamond, trapezoidal and I-beam), the depth profile is essentially similar (not shown). The CFD prediction of velocity profiles (Fig. 7b) are also in good agreement with the measurements (by propeller current meter).

#### 4.4. Air concentration of air–water flow downstream of rack interception

Fig. 8a shows the computed flow profiles and air concentration (c) between the racks in the longitudinal section of the open channel flow downstream of rack interception ( $Q = 41.3$  L/s, circular rack). Fig. 8b shows the computed and measured air concentration profiles normal to

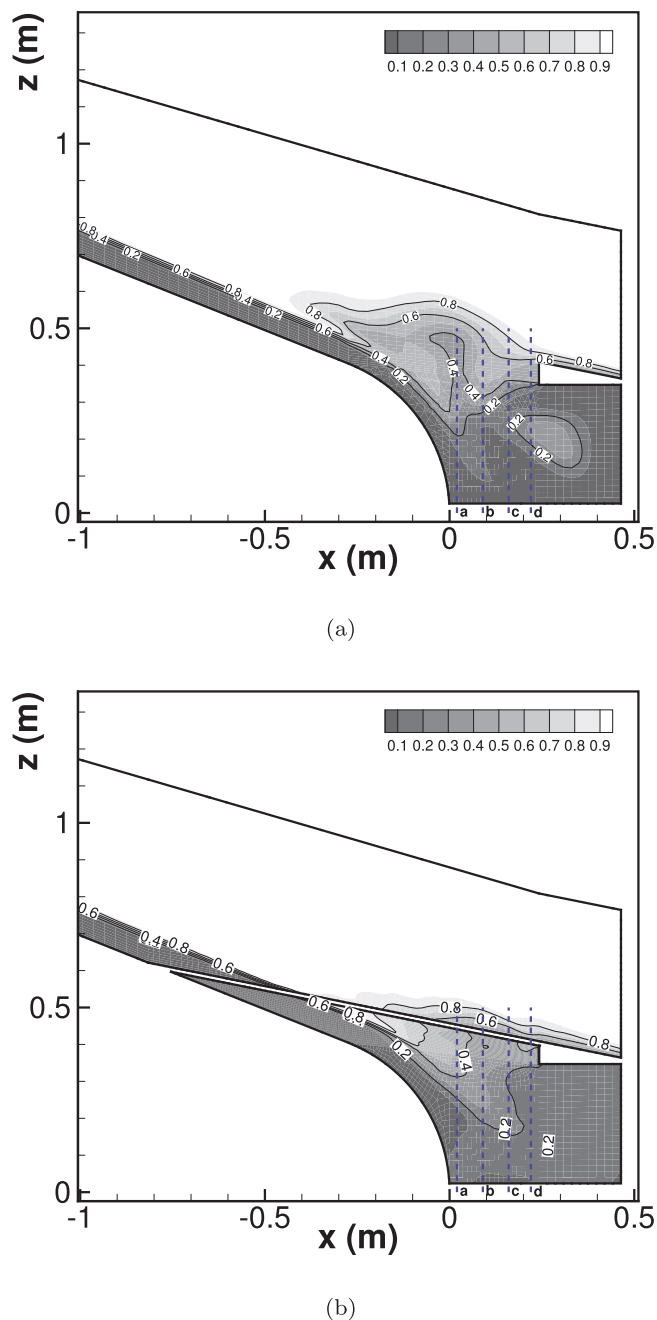


Fig. 12. CFD predicted average air concentration distribution along centerline of bottom rack chamber for high flow ( $Q = 70.5$  L/s), (a) without rack, (b) circular-bar rack.

the channel at various  $x$ -sections. The bottom layer of the main channel flow is in clear water ( $c = 0$ ). Above the clear water layer, the air concentration increases to 1.0 over a transition layer of air–water mixture that grows with distance from rack interception. The measured air concentration in the complex and highly fluctuating flow is a result of the entrained air, the unsteady nature of the jet–water boundary of the underflow and sheet jet, and droplets due to the flow impingement and splashing. A nominal thickness of the mixed air–water layer can be defined as the region of  $1\% < c < 50\%$ . In general our measurements show that the measured air concentration profile ‘between the rack bars’ and ‘beneath the rack’ are similar. For  $Q = 41.3$  L/s, both CFD calculations and measurements show that the surface aerated layer thickness is around 15–20 mm, while the clear water layer depth is around 30 mm. The air concentration measurement for a case without-

rack at  $Q = 41.3$  L/s (not shown) reveals only slightly smaller surface aerated layer thicknesses, indicating that the sheet jet does not affect the flow aeration significantly (see discussion below). Over the range of flows tested, the thickness of the aerated layer remains more or less constant – reflecting the weak dependence of velocity on unit discharge (not shown).

#### 4.5. Air–water flow inside the bottom rack chamber

Fig. 9a and b show the predicted and observed characteristic flow features inside the bottom rack chamber for a medium flow condition ( $Q = 43.1$  L/s). Upstream of the bottom rack, the approach flow is uniform with small air entrainment (Fig. 9a). Due to acceleration, change of flow direction and air entrainment, the flow inside the bottom rack chamber is 3D, highly turbulent and aerated. The intercepted flow follows the bottom slope and enters stably into the chamber. The bottom part of this flow hits the far end of the chamber and is re-directed inside the chamber. An anti-clockwise circulation is formed in the chamber (Figs. 9b and 10). The momentum of the top part of the chamber flow is partly offset by the opposing channel inflow. The instantaneous air concentration is highly non-uniform; however, the air concentration is generally higher at the start of the curved bottom – where the wall jet impinges onto the recirculating spiral circulation (Fig. 10). The jet impingement on the chamber circulation gives rise to intense turbulence and energy dissipation; in fact this is a characteristic feature of the design to maximize energy dissipation and to stabilize and re-direct the flow by  $90^\circ$  onto the link channel leading into the vortex intake.

The average air concentration distribution at the bottom rack chamber can be evaluated by averaging the predicted air volume fraction at an snap-shot interval of 0.1 s for a total simulation period of 20 s assuming a quasi-steady flow. At low flow,  $Q = 23.6$  L/s (Fig. 11), the inflow plunges into the chamber as a highly fluctuating high velocity jet. As the water stream plunges onto the water inside the chamber, air entrainment occurs. The surface level of water in the chamber is highly unsteady and 3D. At the closed downstream end of the chamber, a ‘water-dune’ is formed as the inflow hits the chamber wall. Note that for the case without the bottom rack, a core of higher air concentration is formed at the center of the chamber due to the anti-clockwise circulation (Fig. 11a), while in the case with a bottom rack, the air concentration is more dispersed, due to the increase in turbulence level induced by the rack (Fig. 11b).

At high flow of  $Q = 70.5$  L/s (Fig. 12), the bottom rack chamber is surcharged; some of the air–water mixture splashes up from the chamber and drains onto the overflow channel downstream (Fig. 12a). The bottom rack acts to dampen the free surface fluctuation and spillage of water from the chamber (Fig. 12b).

Fig. 13a and b compares the measured and CFD predicted vertical profiles of time-averaged air concentration (volume fraction) at different sections for the low flow case. Both computed and measured air concentration profiles show a distinct vertical gradient, with air concentrations of around 0.3 to 0.5 in the center of the chamber resulting from the air entrainment. In general the effect induced by the bottom rack appears to be not significant, as air entrainment is mainly induced by the impingement of the plunging bottom rack flow and the wall jet onto the chamber circulation. The CFD model predictions compare well with measurements at location close to the interception point ( $x = 20$  and  $90$  mm) but a higher air concentration is predicted throughout the depth at a location further from the interception point ( $x = 160$  mm). In both cases of circular and diamond bars, the air concentration pattern is similar (not shown).

In contrast, for the high flow case (Fig. 13c, d), the bottom rack flow is much less aerated; the time scale for diffusion of air into the water is much less and there is a lack of air–water interfaces for air-entrainment; hence the air concentration in the chamber is visibly less than that of the lower flow case ( $< 25\%$ ). The air concentration is low below a

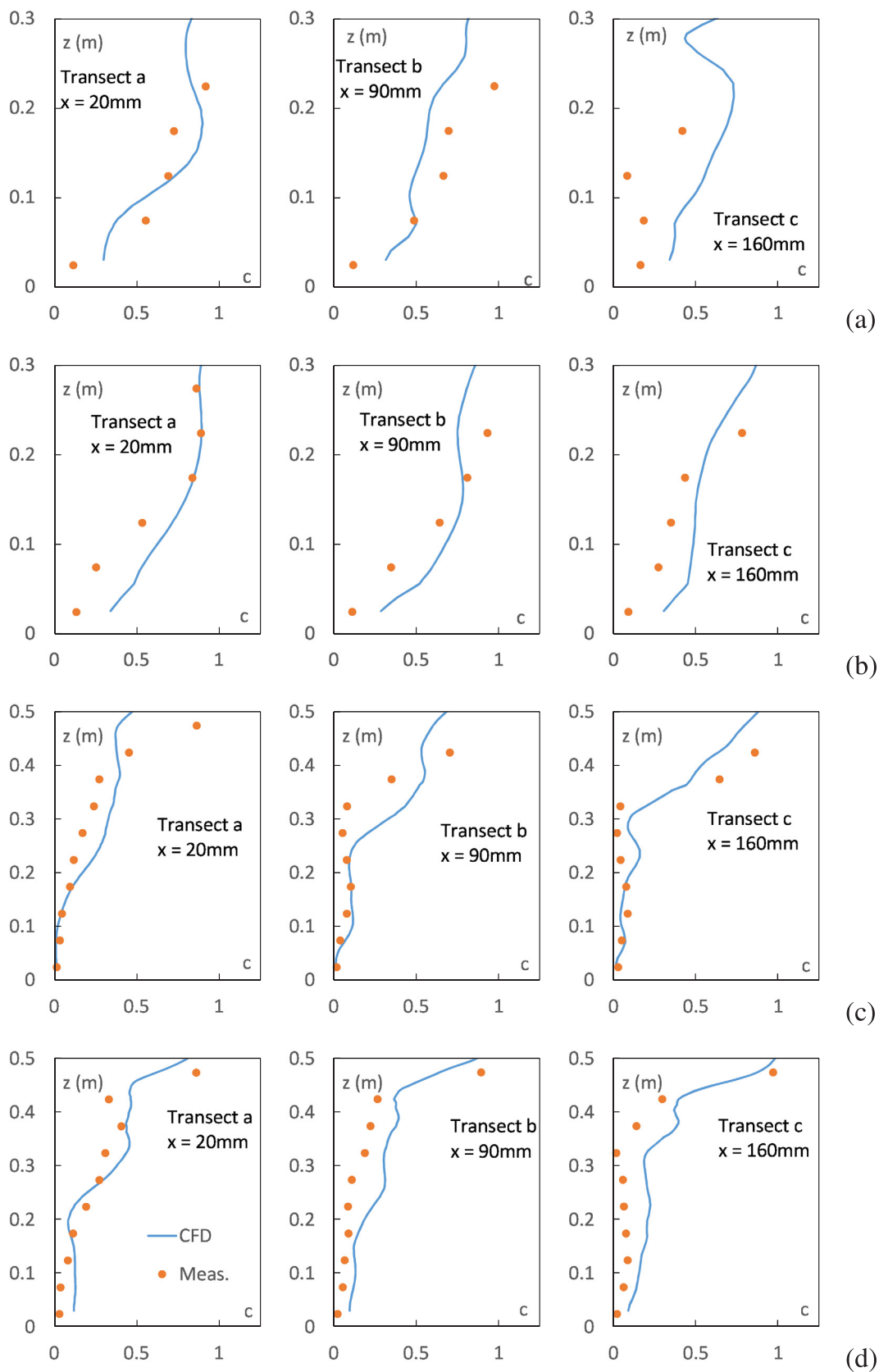


**Fig. 13.** Comparison of predicted and measured air concentration at the bottom rack chamber: (a) low flow ( $Q = 23.6$  L/s), without rack; (b) low flow, circular-bar rack; (c) high flow ( $Q = 70.5$  L/s), without rack; (d) high flow, with circular-bar rack.  $x = 0$  refers to the toe of curved channel at the bottom of chamber. Transects a, b and c are shown in Fig. 11.

**Table 2**  
Comparison of measured and predicted volume average air concentration (%) in rack chamber for cases (a) without-rack, (b) with circular rack and (c) with diamond rack.

Discharge Q (L/s)	(a) Without-rack		(b) Circular rack		(c) Diamond rack	
	Measured	CFD	Measured	CFD	Measured	CFD
23.6	46.1	54.3	47.3	59.6	41.0	60.5
45.8	29.8	29.7	30.1	34.2	32.2	33.5
70.5	20.2	24.2	19.7	26.2	20.0	26.3

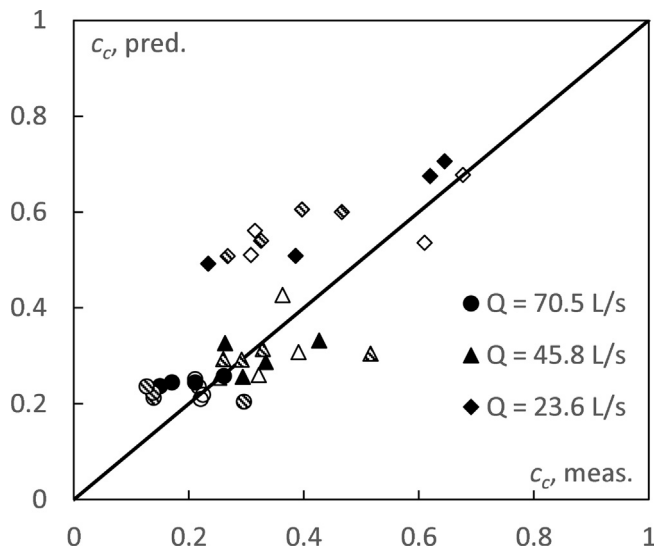


**Fig. 14.** Comparison of predicted and measured vertically-averaged air concentration  $C_c$  at different transects in centerline plane. Open symbol: without rack; solid symbol: circular rack; shaded symbol: diamond rack.

level of  $z = 0.3$  m. Above  $z = 0.35$  m, the air concentration increases sharply, indicating a fluctuating free surface. The case with a bottom rack shows a slightly higher air volume fraction, indicating the effect of rack bars in increasing air entrainment (Fig. 13d). The model prediction compares satisfactorily with measurement.

The depth-averaged air concentration ( $\bar{c}_c$ ) on a vertical transect (transects a to d; see Fig. 11) is defined as:

$$\bar{c}_c = \frac{c_1 + c_2 + c_3 + \dots + c_n}{n} \tag{5}$$

where  $c_1, c_2, c_3, \dots, c_n$  are the individual concentration measurements and  $n$  is the number of measurements on each transect. For the centerline plane (for which air concentration measurements are made), a plane-averaged ( $\bar{c}_p$ ) air concentration is calculated as:

$$\bar{c}_p(y) = \frac{\bar{c}_{c,a} + \bar{c}_{c,b} + \bar{c}_{c,c} + \bar{c}_{c,d}}{4} \tag{6}$$

The volume-averaged air concentration is calculated from the plane average by:

$$\bar{c}_v = \frac{\bar{c}_{p,A} + \bar{c}_{p,B} + \bar{c}_{p,C}}{3} \tag{7}$$

where A, B, C are the vertical planes at  $y = 0.03$  m (near chamber outlet), 0.158 m (channel centerline) and 0.275 m, respectively.

Table 2 shows a summary of predicted and measured volume-averaged ( $\bar{c}_v$ ) air concentration for different flow rates and bar shapes (without rack, circular and diamond shaped bars). Supported by the numerical model predictions, the measured volume-averaged air concentration ranged from 20% to 50%; the air concentration for  $Q = 70.5$  L/s is less than half of the lowest discharge ( $Q = 23.6$  L/s). For

low flow condition, where the intensive air entrainment is induced by the plunging flow from the approach channel into the rack chamber, the model over-predicts the air concentration by 18–26 % for the without rack and circular rack cases respectively; the discrepancy is greater (about 48%) for the diamond shaped bars. On the other hand, for the high flow case,  $Q = 70.5$  L/s, the error is around 20–30 % for all three rack scenarios. The least discrepancy (less than 10%) is found for the intermediate flow case,  $Q = 45.8$  L/s. This shows the challenges in modeling complex air–water flows using VOF method, where there is no clear interface between air and water.

Fig. 14 shows the comparison of predicted and measured vertically-averaged air concentration for the different transects in the centerline plane. Given the highly unsteady nature of the complex flow in the bottom rack chamber, the comparison of averaged air concentration for each measurement line is encouraging. The highest discrepancy occurs for low flow where air entrainment is significant. Overall, it is concluded that bottom rack bars does not have a significant effect on air entrainment in the rack chamber.

### 5. Concluding remarks

The hydraulics of a supercritical bottom rack intake has been studied using a physical model and 3D CFD VOF simulation. The major findings are summarized as follows:

- The supercritical flow depth above the rack increases in the flow direction due to energy losses resulting from flow contraction and expansion during flow passage through the racks. For  $x_s \leq 0.75 L_w$ , the free surface profile is well-predicted by the Gradually-varied flow theory using the Standard Step Method. As the flow nearly passes the rack, the flow depth decreases abruptly and three dimensional effects play a dominant role.
- The supercritical flow passes through the racks and forms an underflow beneath them; a sheet jet formed by the rack bars plunges onto the main channel flow. The plunging induces roughness on the underflow but does not cause significant air entrainment.
- The flow features in the rack chamber and the air concentration field are studied both with and without rack presence. In general, the highly fluctuating flow consists of a wall jet impinging onto a spiral circulating flow in the chamber. The jet impingement generates significant turbulent kinetic energy and air entrainment. The air concentration decreases with increasing discharge. The general chamber flow structure appears to be little affected by the presence of the bottom rack or the shape of rack.
- CFD predictions of the free surface level above the rack, major flow features beneath the rack and average air concentration compare well with experimental measurements. However, detailed flow features such as the sheet jet beneath the rack cannot be satisfactorily simulated. Video clips of the bottom rack flow can be downloaded from the [Supplementary Materials](#).

The system of 34 bottom rack chambers and vortex intakes have been successfully implemented in the HKWDT scheme to alleviate flood risks in the urban areas of Hong Kong. Since its commissioning in 2012, stormwater runoff from over 500 hectares uphill catchment during every heavy downpour (up to 230 mm daily rainfall) has been successfully intercepted by the system with no downstream urban flooding.

### Acknowledgment

This study was supported by the Drainage Services Department of the Hong Kong SAR Government and in part by a grant from the Hong Kong Research Grants Council (RGC 714306).

## Appendix A. Supplementary data

Supplementary data associated with this article can be found, in the online version, at <https://doi.org/10.1016/j.jher.2018.08.001>.

## References

- ANSYS Inc., 2013. ANSYS FLUENT 15.0 Theory Guide. ANSYS, Canonsburg, PA.
- Bayon, A., Toro, J.P., Bombardelli, F.A., Matos, J., Lopez-Jimenez, P.A., 2017. Influence of VOF technique, turbulence model and discretization scheme on the numerical simulation of the non-aerated, skimming flow in stepped spillways. *J. Hydro-Environ. Res.* <https://doi.org/10.1016/j.jher.2017.10.002> (in press).
- Bombardelli, F.A., Hirt, C.W., Garcia, M.H., 2001. Discussion on computations of curved free surface water flow on spiral concentrators. *J. Hydraul. Eng., ASCE* 127 (7), 629–631.
- Bombardelli, F.A., Meireles, L., Matos, J., 2011. Laboratory measurements and multi-block numerical simulations of the mean flow and turbulence in the non-aerated skimming flow region of steep stepped spillways. *Environ. Fluid Mech.* 11 (3), 263–288.
- Brunella, S., Hager, W.H., Minor, H.-E., 2003. Hydraulics of bottom rack intake. *J. Hydraul. Eng., ASCE* 129 (1), 2–10.
- Castillo, L.G., Carrillo, J.M., Garcia, J.T., 2013. Flow and sediment transport through bottom racks – CFD application and verification with experimental measurements. In: *Proceedings of 2013 IAHR Congress, Chengdu, China, Sep 2013*. Tsinghua University Press, Beijing, China.
- Chan, S.N., Cong, J., Lee, J.H.W., 2018. 3D numerical modeling of geyser formation by release of entrapped air from horizontal pipe into vertical shaft. *J. Hydraul. Eng.* 144 (3), 04017071.
- Drainage Service Department (DSD), 2003. Stormwater Drainage Master Plan Study in Northern Hong Kong Island – Executive Summary. The Government of Hong Kong Special Administrative Region, Hong Kong, China.
- Hager, W.H., Minor, H.-E., 2003. Hydraulic design of bottom rack intakes. *Proc. 30th IAHR Congress, Thessaloniki, Greece, 495–502*, IAHR, Madrid, Spain.
- Henderson, F.M., 1966. *Open Channel Flow*. Macmillan, New York.
- Hirt, C.W., 2003. Modeling turbulent entrainment of air at a free surface. FSI-03-TN61-R. Flow Science Inc, Santa Fe, NM, USA.
- Hirt, C.W., Nichols, B.D., 1981. Volume of fluid (VOF) method for the dynamics of free boundaries. *J. Comput. Phys.* 39 (1), 201–225.
- Kumar, S., Ahmad, Z., Kothiyari, U.C., Mittal, M.K., 2010. Discharge characteristics of a trench weir. *Flow Meas. Instrum.* 21, 80–87.
- Lee, J.H.W., Chan, H.C., Yu, D.Y., Choi, D.K.W., 2005a. Physical hydraulic model tests for Hong Kong West Drainage tunnel in Northern Hong Kong Island – Intake Structure, Final Report to Drainage Services Department, HKSAR Government, February 2005, 104 pp.
- Lee, J.H.W., Yu, D., Chan, H.C., Gore, L., Ackers, J., 2005b. Bottom rack intake for supercritical storm flow diversion on steep urban catchment. *Proceedings of the 31st IAHR World Congress, Seoul, Korea*. The International Association for Hydro-Environment Engineering and Research, Madrid, Spain.
- Lee, J.H.W., Yu, D., Chan, H.C., Ackers, J., Gore, L., 2006. Experimental study on supercritical vortex intakes for urban drainage diversion. *Proceedings of the Eleventh Asian Congress of Fluid Mechanics, 22–25 May 2006, Kuala Lumpur, Malaysia*.
- Meireles, L., Bombardelli, F.A., Matos, J., 2014. Air entrainment onset in skimming flows on steep stepped spillways: an analysis. *J. Hydraul. Res.* 52, 375–385.
- Mostkow, M.A., 1959. Theoretical study of bottom type water intake. *La Houille Blanche* 4, 570–580.
- Righetti, M., Lanzoni, S., 2008. Experimental study of the flow field over bottom intake racks. *J. Hydraul. Eng., ASCE* 134 (1), 15–22.
- Subramanya, K., 2009. *Flow in open channels*, third ed. Tata McGraw-Hill, New Delhi.
- Valero, D., Bung, D.B., 2015. Hybrid investigation of air transport processes in moderately sloped stepped spillway flows. *Proceedings of the 36th IAHR World Congress, the Hague, the Netherlands*. The International Association for Hydro-Environment Engineering and Research, Madrid, Spain.
- Wong, K.C., 2009. *Hydraulics of Bottom Rack Chamber for Supercritical Flow Diversion*. M.Phil Thesis. The University of Hong Kong, Hong Kong, China.
- Yakhot, V., Orszag, S.A., Thangam, S., Gatski, T.B., Speziale, C.G., 1992. Development of turbulence models for shear flows by a double expansion technique. *Phys. Fluids A* 4 (7), 1510–1520.